



Numerical contribution to segmented chip effect on residual stress distribution in orthogonal cutting of Inconel718

Yang Liu¹ · Mathias Agmell¹ · Dongdong Xu² · Aylin Ahadi¹ · Jan-Eric Stahl¹ · Jinming Zhou¹

Received: 24 March 2020 / Accepted: 30 June 2020 / Published online: 10 July 2020
© The Author(s) 2020

Abstract

Segmented chip morphology has a significant influence on distribution of residual stress and surface topography on machined surface in machining difficult-to-cut materials. In this paper, Coupled Eulerian and Lagrangian (CEL) model is employed to investigate the effect of segmented chip on surface integrity (residual stress distribution and surface topography) in orthogonal machining of Inconel718 with uncoated carbide inserts. A mesh sensitivity study of chip morphology and residual stress distribution is performed by developing the following three different grid resolutions: coarse (mesh size 35 μm), medium (10 μm) and fine (5 μm). Comparing with the experimental results, it is clear that the numerical model presents reasonable results, including the chip morphology, temperature distribution, cutting forces, residual stress profile and surface fluctuation period. As for the generated surface integrity, a waved surface and cyclic residual stress distribution are found with the segmented chip due to the periodical mechanical and thermal loadings acting on the machined surface. Furthermore, the formation of single chip segment is investigated in-depth to explain the residual stress distribution generation.

Keywords CEL · Segmented chip · Residual stress · Surface topography · Inconel718

1 Introduction

Nickel-based superalloy (e.g. Inconel718) is widely used for safety critical components manufacturing (e.g. jet engine and high-speed airframe parts) due to its high strength, corrosion resistance, weldability and long-term stability at elevated temperature. However, these excellent properties for applications have made it difficult to machine this group of materials. The surface integrity, especially the residual stress left in the machined part, is one of the most concerns when manufacturing difficult-to-cut materials, which has detrimental or favourable effects on the component life and functional behaviour. Finite element method has been proven to be effective to capture various aspects of the

machining process simultaneously, such as cutting forces [1], chip morphology [2], temperature distribution [3], plastic deformation zones [4], cutting tool stress distribution [5, 6], contact length [7], residual stress [8] and microstructural changes in the material [9].

The commonly used FE method for metal cutting simulation can be categorized into Lagrangian, updated Lagrangian, Arbitrary Lagrangian-Eulerian and Coupled Eulerian and Lagrangian. When using Lagrangian formulation, a damaged layer with a separation criterion is typically used to separate chips from workpiece. However, the stress and strain distributions on the machined surface are significantly affected by the magnitude of the separation criteria [10]. A trial and error method should be adopted to determine the magnitude of the separation criteria which adds a large degree of uncertainty into the model. In addition, the high distorted element reaching the damage criterion will be deleted during the simulation, resulting in the absence of higher value of temperature, stress and strain material, thus to reduce the accuracy of the results [11]. In updated Lagrangian formulation (re-meshing) [4, 12–14], interpolation will be employed during the mapping process where the solution data are transferred from old distorted mesh to the new mesh, while the accuracy of results will be deteriorated after repetitive re-meshing occurred. Regarding the Arbitrary Lagrangian-Eulerian

✉ Yang Liu
yang.liu@iprod.lth.se

✉ Dongdong Xu
dongdong.xu2@nottingham.ac.uk

¹ Division of Production and Materials Engineering, Lund University, Box 118, Lund, Sweden

² Institute of Aerospace Technology, University of Nottingham, Nottingham NG7 2TU, UK

(ALE), the topology (elements and connectivity) of the mesh cannot be altered through the entire simulation, which limits the ability of this method to maintain a high-quality mesh upon extreme deformation. Currently, there are two types of boundary conditions applied in ALE, which are combined Eulerian and Lagrangian [15–20] and pure Lagrangian boundary, while only Lagrangian boundary can generate segmented chip. However, according to Ducobu et al. [3], the segmented chip morphology obtained using this method was proven to be far from the experimental one or that from a Lagrangian simulation.

To solve the above-mentioned problems, Coupled Eulerian Lagrangian (CEL) formulation has been developed and is becoming a competitive method to guarantee both the accuracy of the results and segmented chip generation [21]. In the CEL model, the workpiece undergoing large deformation is meshed with Eulerian formulation where the material and the mesh are independent, while the cutting tool is modelled by Lagrangian formulation. The fixed elements in Eulerian part can be void, partially occupied or fully occupied by material, thus element distortion can be totally avoided. When comparing with the ALE method, it has been proved that [22, 23] the chip morphology and cutting forces from the CEL model were more similar to the experimental one when cutting Ti6Al4V, and avoidance of mesh deformation in the CEL simulation leads to a decrease in computing time. The CEL method has been successfully used in metal cutting simulations by many studies [21, 24, 25] with promising results as well.

The segmented chip is the typical chip morphology when machining difficult-to-cut materials, which is generally believed harmful for cutting tools and surface integrity [26, 27] due to the fluctuation of thermal and mechanical loadings it causes. However, most of the previous studies have been carried out to investigate the effects of tool geometries and cutting conditions on final surface integrity without regard to the influence of segmented chip. The influence of the segmented chip formation of AISI 316L on the periodic loads acting on the cutting tool has been investigated by Mathias et al. [21], but it did not address

Table 1 Constants of the Johnson-Cook constitutive model for Inconel718 [36]

Material	A (MPa)	B (MPa)	n	C	m
Inconel718	1377	1243.5	0.6767	0.0045	1.29

much about machined surface integrity. It was reported that [28] the remarkable deviation in the magnitude and distribution of the residual stress induced by machining titanium with different chip morphology was attributed to the substantial difference in temperature and cutting forces generated in the cutting process. However, how the segmented chip morphology affects temperature and cutting forces have not been explained. A rippled surface and a cyclic evolution of residual stress in the machined aeronautic aluminium alloy with a generated segmented chip were found [29], but the relationship between the segmented chip and machined surface integrity was still unclear. It is well known that the mesh size will significantly affect the simulation accuracy; therefore, the mesh size influence investigation is necessary when doing the simulation. When it comes to the mesh influence using the CEL method, Ducobu et al. [30] investigated the effect of the element size and orientation on the results (chip morphology, temperatures and forces) in the orthogonal cutting process, but it was based on the continuous chip and not related to residual stress prediction.

As discussed previously, although it is of significant importance, the relationship between the segmented chip and surface integrity has not been clearly addressed and the mesh dependency in segmented chip generation with CEL method has not been revealed. In this study, both the finite element model based on the CEL formulation and experimental investigation are used to provide detailed information about the surface integrity (residual stress distribution and surface topography) induced by orthogonal cutting of Inconel718. The mesh dependency issue is highlighted when the CEL is adopted to get the appropriate simulated segmented chips and accurate surface topography. The

Fig. 1 Schematic initial geometry and boundary conditions of the model

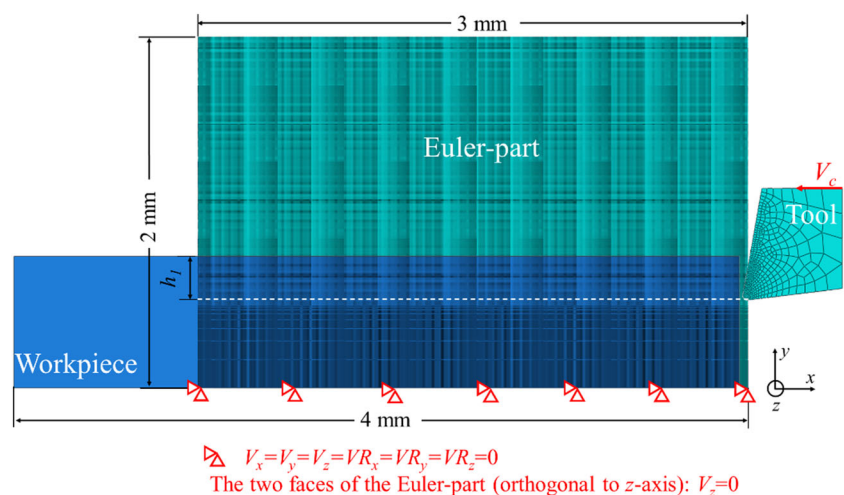


Table 2 Workpiece and tool physical parameters

Properties	Workpiece (Inconel718)	Tool (uncoated tungsten carbide)
Thermal conductivity (W/m°C)	12 (20 °C) 24 (900 °C)	82
Density (kg/m ³)	8221	14,860
Young's modulus E (GPa)	212	600
Poisson's ratio ν	0.294	0.2
Expansion (°C ⁻¹)	1.2e-5 (20 °C) 1.7e-5 (900 °C)	5.2
Inelastic heat fraction	0.9	–
Specific heat (J/kg°C)	440 (20 °C) 680 (900 °C)	249.8
T_{room} (°C)	25	25
T_{melt} (°C)	1344	–

segmented chip influences on the surface integrity are discussed through the analysis of thermal loading and mechanical loadings. Furthermore, the cyclic evolution of the surface integrity is deeply explored based on the investigation of the single chip segment formation and its stress acting on the machined surface.

2 Numerical modelling

2.1 Model based on CEL formulation

The explicit, dynamic, temperature-displacement coupled analysis is implemented using Abaqus/Explicit 6.14-2. The

analysis is done in three steps; the first step simulates the cutting process while the second one removes the tool and followed by the third one where the finished workpiece is cooled down to room temperature. A CEL cutting model with the initial geometry and applied boundary is built (Fig. 1), in which the workpiece is fixed while the tool advances to remove materials at the cutting speed. The Euler part is initially filled with workpiece material in the crossed region of the two parts, while the rest of the Euler space, where the chip will be formed, is regarded as void. It has been reported [30] that the Euler space should be meshed into square elements to avoid the element orientation effect and the mesh width has no influence on the results in two-dimensional simulation. The element type used in the workpiece is EC3D8RT which is an 8-node thermally coupled linear Eulerian brick element, and the tool is defined to be rigid by using an 8-node thermally coupled brick element. It is known that the drastic change of the residual stress is typically observed in the region of around 100 μm of the superficial surface, where it should be finely meshed in y -axis to express the residual stress precisely.

2.2 Material model

In metal cutting simulation, Johnson-Cook constitutive law is the most commonly used material model because it takes into account the effect of material strain and strain rate hardening as well as thermal softening. In the classic constitutive Johnson-Cook laws, flow stress increases with the increasing strain under any temperature and strain rate conditions, which

Fig. 2 The schematic of experimental set-up illustrating the (a) temperature measurement and (b) cutting forces measurement

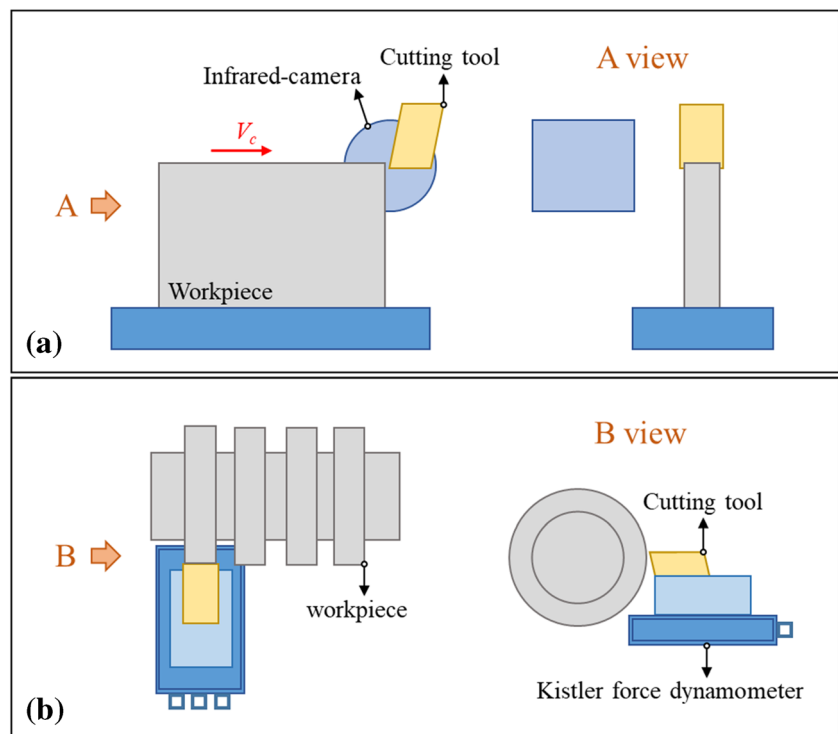


Table 3 Tool geometry and cutting parameters used in the simulation and experiment

Rake angle γ (°)	10
Clearance angle α (°)	7
Flank wear VB_s (mm)	0
Edge radius r_β (mm)	0.025
Insert width (mm)	3.9
Uncut chip thickness h_1 (mm)	0.05, 0.25
Cutting speed V_c (m/min)	40, 80

is invalid in predicting the segmented chip formation due to the absence of flow stress decreasing behaviour (strain-softening phenomenon). Therefore, the damage model and damage evolution model were introduced and combined [31–34] to characterize the strain-softening, while it shows good coherence with the experimental results. Thus, the Johnson-Cook constitutive model, Johnson-Cook damage model and Hillerborg’s fracture energy model are adopted in the present study to predict strain hardening, strain softening, thermal softening and strain rate hardening behaviour of Inconel718.

2.2.1 Constitutive model

Johnson-Cook flow stress rule [35] is expressed as Eq. (1),

$$\bar{\sigma} = \left[A + B(\bar{\epsilon})^n \right] \left[1 + C \ln \left(\frac{\dot{\bar{\epsilon}}}{\dot{\bar{\epsilon}}_0} \right) \right] \left[1 - \frac{T - T_{room}}{T_{melt} - T_{room}} \right]^m \quad (1)$$

where $\bar{\sigma}$ is the equivalent flow stress; $\bar{\epsilon}$ is the equivalent plastic strain; $\dot{\bar{\epsilon}}$ is the equivalent plastic strain rate; $\dot{\bar{\epsilon}}_0$ is the reference strain rate; T_{melt} is the melting point of material; T_{room} is the room temperature. The Inconel718 used in this study was a solution heat treated (1052 °C) followed by ageing treatment (877 °C), which conforms to the heat treatment condition of Inconel718 specimens in the study [36]. Therefore, it is acceptable to assume the parameters of A , B , n , C and m constant, listed in Table 1, which are determined in the compression test [36]. Workpiece and tool physical parameters are listed in Table 2.

Fig. 3 Chip morphology obtained from (a) experiment and simulation with (b) coarse mesh, (c) medium mesh, and (d) fine mesh under condition of $V_c = 80$ m/min, $h_1 = 0.25$ mm

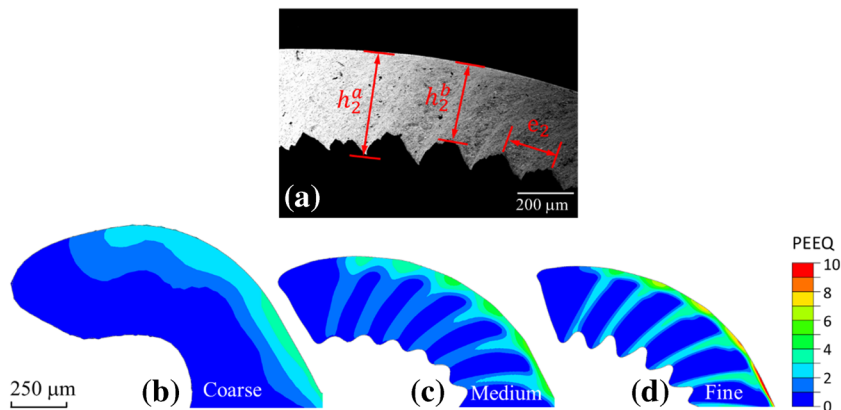


Table 4 Segmented chip morphology comparison between simulation and experiment

Parameters	h_2^a (μm)	h_2^b (μm)	e_2 (μm)	f_s (kHz)
Experiment	380	278	173	5.61
Fine	378 (-0.5%)	289 (4.0%)	165 (-4.6%)	5.88 (4.8%)
Medium	345 (-9.2%)	300 (7.9%)	99 (-42.8%)	9.79 (74.5%)

2.2.2 Strain softening criterion

The criterion used to identify the damage initiation is the Johnson-Cook damage model [37]. The material starts to damage when its equivalent plastic strain reaches to $\bar{\epsilon}_0$ which is defined by Eq. (2),

$$\bar{\epsilon}_0 = \left[D_1 + D_2 \exp \left(D_3 \frac{P}{\bar{\sigma}} \right) \right] \left[1 + D_4 \ln \left(\frac{\dot{\bar{\epsilon}}}{\dot{\bar{\epsilon}}_0} \right) \right] \left[1 + D_5 \left(\frac{T - T_{room}}{T_{melt} - T_{room}} \right) \right] \quad (2)$$

where $D_{i(i=1-5)}$ are five constant failure parameters and p is hydrostatic stress.

A given element begins failure when scalar damage parameter ω , cf. Eq. (3), exceeds one,

$$\omega = \sum_{i=1}^n \left(\frac{\Delta \bar{\epsilon}}{\bar{\epsilon}_0} \right)_i \quad (3)$$

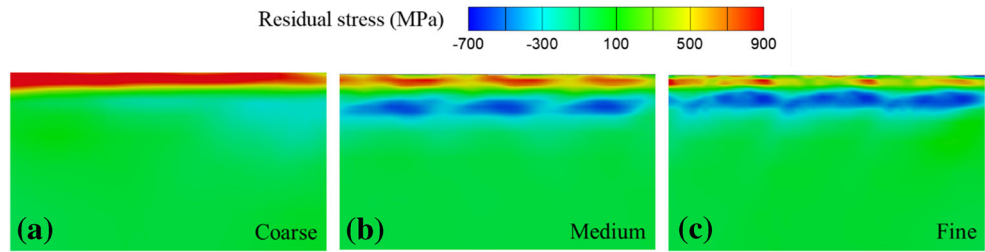
where $\Delta \bar{\epsilon}$ is the increment of equivalent plastic strain at unit integration point during an increment, i .

In the damage evolution stage, Hillerborg’s fracture energy G_f [38] is introduced to describe the energy dissipated during the damage evolution process,

$$G_f = \int_{\bar{\epsilon}_0}^{\bar{\epsilon}_f} L \tilde{\sigma} d\bar{\epsilon} = \int_0^{\bar{u}_f} \tilde{\sigma} d\bar{u} \quad (4)$$

where, L is the characteristic length associated with an integration point; $\tilde{\sigma}$ is the flow stress in this stage; $\bar{u} = L\bar{\epsilon}$ is the

Fig. 4 Residual stress distribution with different mesh sizes under condition of $V_c = 80$ m/min, $h_1 = 0.25$ mm: (a) Coarse mesh, (b) Medium mesh, and (c) Fine mesh



equivalent plastic displacement which is set to zero before damage in Abaqus; $\bar{\epsilon}_f$ and \bar{u}_f are the equivalent plastic strain and the equivalent plastic displacement when the material is totally fractured, respectively. The fracture energy G_f of Inconel718 is offered as an input parameter by $G_f = K_c^2(1 - \nu^2)/E$, where K_c is the fracture toughness.

The stiffness degradation D during material softening process is in the range of 0–1 which is defined as Eq. (5),

$$D = 1 - \exp\left(-\int_0^{\bar{u}} \frac{\bar{\sigma}}{G_f} d\bar{u}\right) \tag{5}$$

After the end of material softening, the plastic equivalent stress σ evolution is given by Eq. (6),

$$\sigma = (1 - D)\bar{\sigma} \tag{6}$$

where $\bar{\sigma}$ is the stress in the material if it would be undamaged. The parameters of $\bar{\epsilon}_0$ and D are adjusted to achieve a good comparison of chip morphology and cutting forces with the experimental data [39]. In this study, $\bar{\epsilon}_0$ and D are set to be 0.9 and 0.6, respectively.

2.3 Friction and heat modelling

The combination of the Coulomb’s and shear friction model [40] is adopted to capture both the sticking and the sliding behaviour at the tool–chip interface, Eq. (7),

$$\tau_f = \min(\mu\sigma_n, \tau_y) \tag{7}$$

where τ_f is the frictional stress; σ_n is the normal stress between two contact surfaces; τ_y is the yield shear stress of the workpiece material which is defined as $\tau_y = \sigma_y/\sqrt{3}$ where σ_y is the yield stress; μ is the friction coefficient which is defined as Eq. (8) [41],

$$\mu = \frac{F_c \tan \gamma - F_f}{F_c - F_f \tan \gamma} \tag{8}$$

where F_c and F_f are the mean cutting force and mean feed force which can be obtained in the experiment, respectively. Here, μ is equal to 0.66.

The heat generated in the metal cutting process is mainly from plastic deformation in deformation zones and friction in

the tool/workpiece interface. The fraction of the heat converted from plastic deformation work is 0.9. The heat generated by friction is considered to be totally absorbed by the material. Since the cutting process is so fast that heat transfer to environment would be limited, the cutting stage can be treated as adiabatic. In the cooling down stage, workpiece and tool are allowed to exchange heat with the environment. The film coefficient is 100 W/m²°C. The influence of phase transformations on residual stress distribution is assumed to be disregarded.

3 Experimental setup

Orthogonal cutting tests were implemented in dry condition as shown in Fig. 2a, where a solution treated and aged nickel-based superalloy (Inconel718; hardness of 45HRc) with the dimension of 32 mm × 3.25 mm × 30 mm was employed as the workpiece, while a customized uncoated carbide insert CC263 (SECO tools) was used. In addition, the infrared camera FLIR x6580sc with the frame rate of 650 Hz and the integration time of 0.061 ms were used to measure the cutting temperature during the machining process. The detailed cutting parameters and tool geometry can be found in Table 3. The chip produced by the experiment was collected for analysing with scanning electron microscope (SEM), and corresponding machined surface topography was observed with the help of Alicona Infinite Focus Optical 3D microscope. Residual stress distribution in both machined

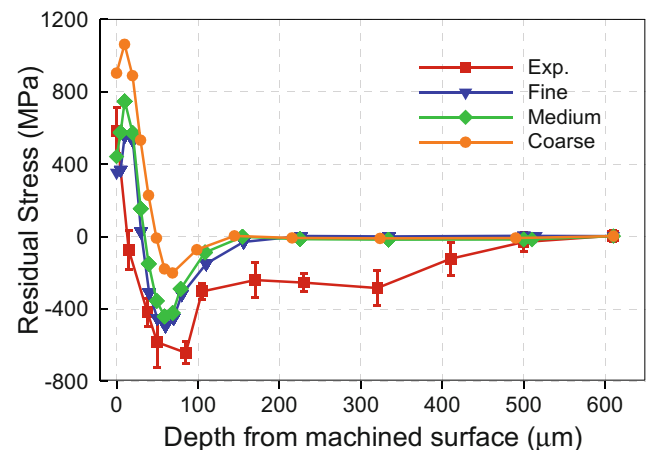
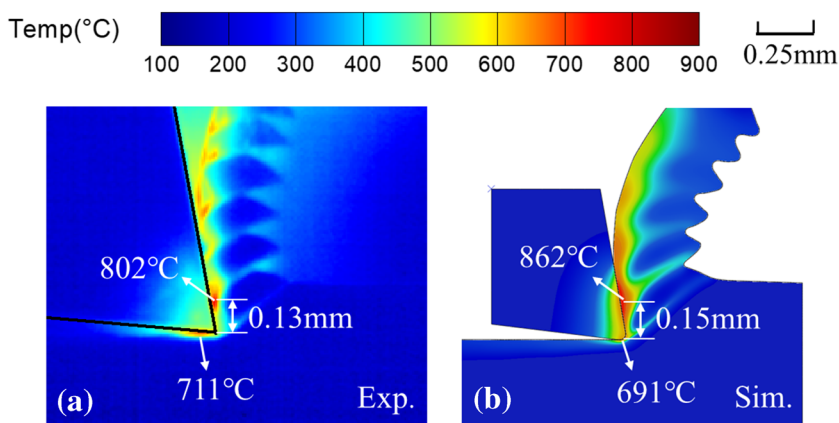


Fig. 5 Experimental and numerical residual stress comparison under condition of $V_c = 80$ m/min, $h_1 = 0.25$ mm

Fig. 6 Temperature distribution from (a) experiment and (b) simulation under condition of $V_c = 80$ m/min, $h_1 = 0.25$ mm



workpiece surface and subsurface was inspected by X-ray diffraction technique using $\sin^2\psi$ method with the help of electropolishing technique. In order to measure the cutting force and feed force, the additional experiment was carried out as shown in Fig. 2b, in which the forces were measured with a Kistler force dynamometer under the mentioned cutting conditions.

4 Results and discussion

4.1 Model validation

4.1.1 Effect of grid resolution

Figure 3 shows both measured and predicted chip morphology under cutting conditions of $V_c = 80$ m/min, $h_1 = 0.25$ mm. The chip morphology obtained from the experiment shows an evident segmented structure (Fig. 3a) and can be characterized with four parameters [21], the maximum tooth height (h_2^a), the minimum tooth height (h_2^b), the tooth width (e_2) and the chip segmentation frequency (f_s), which is determined according to Eq. (9), where λ_h is the chip compression ratio which can be approximately determined by a hyperbolic function $\lambda_h = 1.291 + 0.021/h_1$.

$$f_s = \frac{V_c 1000}{e_2 \lambda_h 60} \tag{9}$$

In simulation, three different grid resolutions are selected to highlight the influence of element size on the cutting process producing segmented chip. In the coarse grid, a total number of 9500 grid cells (smallest mesh size of 35 μm) is defined at the Euler part, while it is 34,000 (smallest mesh size of 10 μm) for medium mesh and 125,600 (element size of 5 μm) for fine mesh. It is obvious that the chip morphology is profoundly influenced by element size (Fig. 3b–d) that the chip is continuous (with the chip thickness of 363 μm) and highly rough with the coarse mesh while the presence of shear bands is noticed with the medium mesh. Moreover, a rather detailed segmented chip morphology is

formed with the fine mesh indicating that a more dense mesh in the Euler space will lead to a more evident characteristic of serrated morphology. Table 4 shows that a good coherence with experimental chip morphology is obtained using the fine mesh in simulation. All the predicted parameters, in that case, have a result within 5% deviation from the experimental ones.

Figure 4 shows the simulated residual stress distribution in the cutting direction (S11) after unloading and the component cooling down. The residual stress field and surface geometry of the finished component are significantly different whether the chip is continuous or segmented. A relatively homogeneous distribution of residual stress at a comparatively smooth machined surface is observed in the CEL model with a coarse mesh, which gives rise to a continuous chip. A cyclic evolution of residual stress at the finished surface accompanied by a periodically waved surface profile is obtained when the cutting process produces a segmented chip, namely the cases with medium and fine mesh. The waved surface geometry generated by the fine mesh has a profile with valley area and peak area as shown in detail in Fig. 9a.

The residual stress profile is averaged in one period in the two cases producing segmented chips. A total of 20 paths from different locations on the finished surface to the bottom are selected, and the average residual stress curves are calculated for three models (Fig. 5). The results show that the element size in the chip area has a significant influence on the

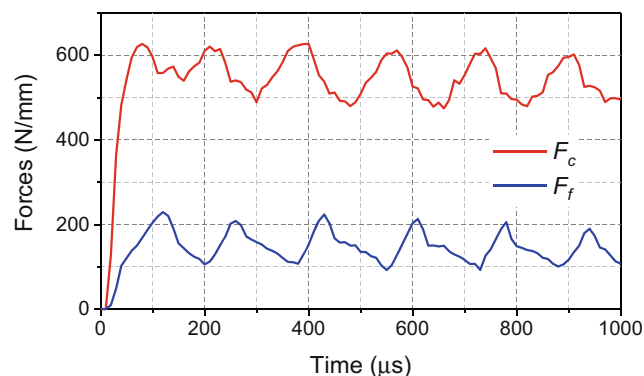


Fig. 7 Cutting forces F_c and feed forces F_f from CEL model under condition of $V_c = 80$ m/min, $h_1 = 0.25$ mm

Table 5 Comparison of average cutting and feed forces between experiment and simulation

Cutting condition	Experiment		Simulation	
	F_c (N/mm)	F_f (N/mm)	F_c (N/mm)	F_f (N/mm)
$V_c = 80$ m/min, $h_1 = 0.25$ mm	575	250	550 (-4.3%)	150 (-40%)
$V_c = 80$ m/min, $h_1 = 0.05$ mm	190	176	150 (-21.1%)	106 (-39.7%)
$V_c = 40$ m/min, $h_1 = 0.05$ mm	200	182	157 (-21.5%)	108 (-40.7%)

residual stress distribution. The tensile residual stress formed in the near-surface layer increase from around 556 MPa with a well-segmented chip from fine mesh to 1062 MPa with a continuous chip from coarse mesh. This is contributed to the absence of material damage in the continuous chip, which will be discussed in the following section. The maximum compressive residual stress below the machined surface increases with more obvious segmented chip simulation. That is likely due to the simultaneous effects of element size in machined workpiece and cutting force variation caused by chip morphology. The results show that the CEL models with medium and fine meshes provide an estimate of the same tendency in in-depth residual stress and almost the same surface magnitude as the measured one.

Consequently, the mesh size is extremely critical in a segmented chip generation model based on CEL formulation, and the fine element size is recommended in this study to obtain accurate information, including chip morphology and residual stress distribution. In the following, the fine mesh will be used as the baseline grid to study the effect of segmented chip on surface integrity.

4.1.2 Temperature distribution

The emissivity of Inconel718 is determined to be 0.2 in this study [42], and the thermography during test was

continuously recorded by an IR camera. Both the measured and predicted temperature distribution at the cutting time of around 2 ms are compared in Fig. 6. Apparently, the numerical simulations replicated the temperature distribution fairly well, in particular numerical simulation predicted successfully the maximum temperature (7.5% difference), the location of the maximum temperature (15.4% difference) and the machined surface temperature (-2.8% difference). In addition, it is noticed that the maximum temperature at the machined surface is not located at the tool tip in experiment, while in simulations, this position is found more close to the tool tip. This is likely due to the growth of flank wear in actual cutting, which did not exist in the simulation.

4.1.3 Cutting and feed forces

Figure 7 shows the evolution of the cutting forces from the simulation. It can be seen that an evident cyclic evolution of the forces is found which is caused by the generation of segmented chips, while the same trend of cutting forces with segmented chip is also observed in [43]. When comparing with the experiment, it can be seen from Table 5 that the CEL model has a better correlation for the cutting force than feed force. A reason for this is due to the simultaneous effects of specified interaction modelling and the rapid tool edge deformation happened in the actual test [44].

Fig. 8 (a) Simulated plastic equivalent strain distribution and (b) measured surface quality under condition of $V_c = 80$ m/min, $h_1 = 0.25$ mm

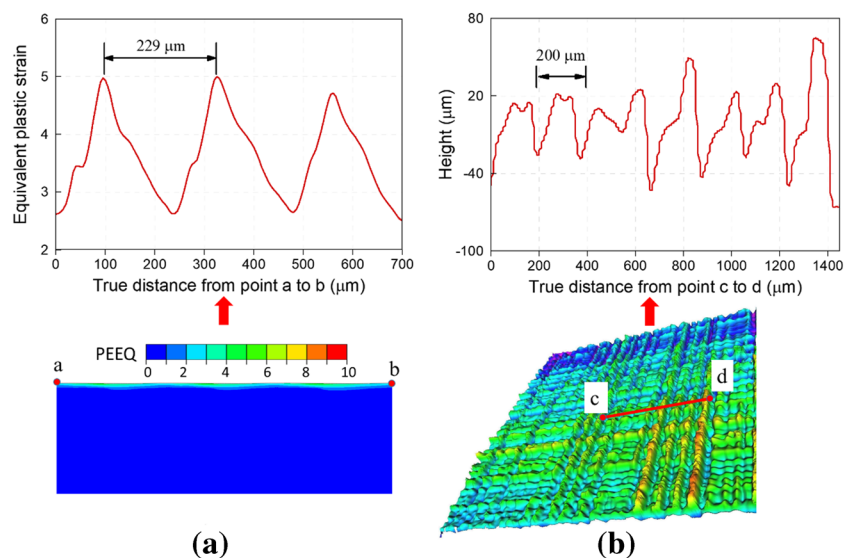
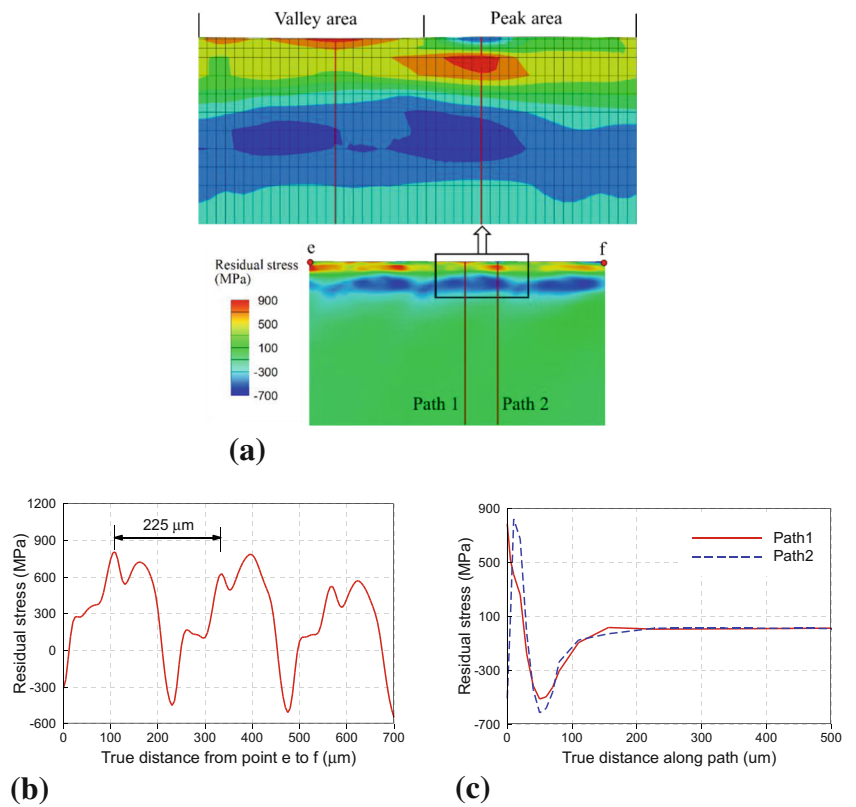


Fig. 9 (a) The close-up picture of residual stress field with fine mesh; (b) residual stress evolution along path e to f; (c) residual stress profile along path 1 and path 2

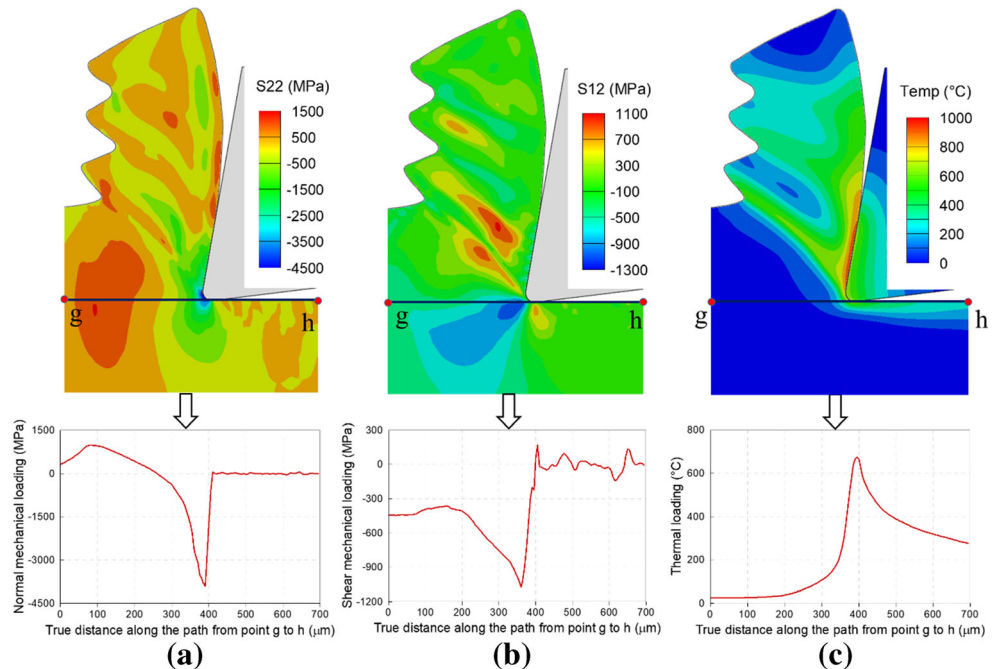


4.1.4 Residual stress and surface topography

To fully validate the numerical model, the predicted residual stress distributions at surface and subsurface are compared with the measured one, which is already shown in Fig. 5. Apart from the deflection caused by the simplicity of the

material model and friction laws, there are four sources of errors in the residual stress determination by means of experiment and simulation. First, residual stress can be introduced unintentionally into the workpiece with various magnitudes and distributions through the manufacturing process. As there are no metallic materials free of residual stress, the residual

Fig. 10 The (a) normal loading, (b) shear loading and (c) thermal loading acting on the machined surface along the loading path



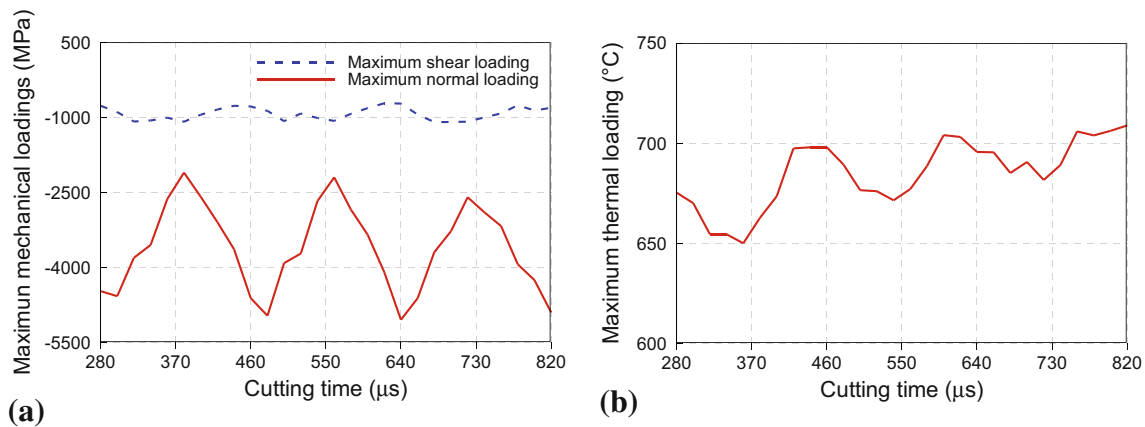


Fig. 11 The evolution of the maximum mechanical and thermal loadings

stress which already exists in the workpiece will more or less affect the residual stress distributions obtained from the experiment. Second, at least one cut is needed to clear the workpiece surface and make it flat before the experiment, which also produces residual stress in the workpiece. Third, due to the elevated temperature and severe deformation suffered by workpiece, complex microstructural changes (twinning, grain refinement, etc.) are generated in the near-surface layer of the workpiece during the cutting process which phenomenon has not been considered in the present simulation. Furthermore, the tool edge would wear or break down during the experiment while a constant tool edge radius would maintain in simulation.

As for the surface topography, the simulated fluctuation period of the waved surface profile can be indicated by the plastic equivalent strain distribution (Fig. 8a). Figure 8b shows the measured machined surface quality and demonstrates that the CEL model provides an acceptable estimation of surface roughness in terms of fluctuation period.

Consequently, the comparison results present good coherence and indicate that the proposed numerical model is capable to simulate the machining process in terms of chip morphology, temperature, forces and surface integrity, showing the possibility to investigate the effect of segmented chip effect on residual stress distribution.

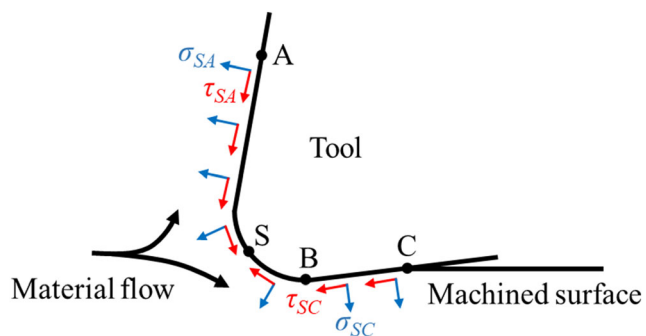


Fig. 12 Schematic view of normal and shear forces acting on the workpiece around stagnation zone

4.2 Effect of the segmented chip on surface integrity

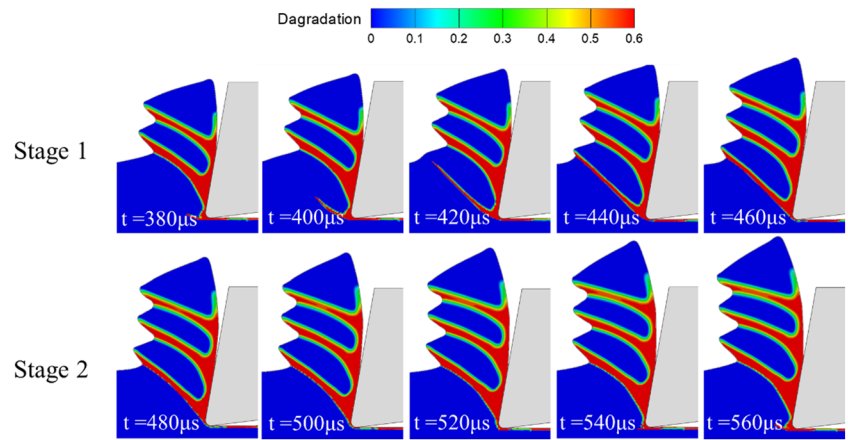
4.2.1 The surface integrity produced by the segmented chip

The following analysis is based on the results from the simulation under condition of $V_c = 80$ m/min, $h_1 = 0.25$ mm because it shows a good agreement with the experimental data. As mentioned previously, a waved machined surface topography accompanied with a periodical residual stress state is noticed with segmented chip. The enlarged pictures show that the residual stress on the machined surface varies from -548 to 803 MPa (Fig. 9b). It can be also seen that the residual stress on the valley locations is much more tensile on the machined surface and less compressive in the sublayer compared with that on the peak zones. The evolutions of the residual stresses versus the workpiece depth in the valley area (path 1) and peak zone (path 2) are detected (Fig. 9c) showing that the residual stress in both path 1 and path 2 is induced up to around 250 μm below the machined surface. Moreover, the tensile residual stress at the valley-shaped surface is stated as 787 MPa and extended to a depth of 25 μm, while the peak compressive stress in this zone is about -511 MPa at a depth of 50 μm below the surface. On the peak zone, the residual stress is compressive only on a very thin surface layer up to 5 μm workpiece depth and becomes tensile up to a depth of 30 μm and finally turn into compressive. Compressive residual stress of -507 MPa is generated on the peaked-shaped surface, followed by a maximum tensile of 823 MPa at a depth of 7 μm and again the peak compressive of -613 MPa penetrating to 50 μm below the surface.

4.2.2 Mechanical and thermal loadings acting on the machined surface

In order to explore the reason that segmented chip leads to such residual stress distribution and surface topography, the mechanical loadings and thermal loading, which can be extracted along a loading path during these processes are

Fig. 13 Distribution of material degradation during one chip segment genesis



investigated. The path from point g to h (Fig. 10) on the finished surface is determined as a loading path, and the corresponding mechanical and thermal loadings along this path at the cutting time of 500 µs are recorded. Figure 11 shows the evolution of maximum value of each loading when cutting time ranges from 280 to 820 µs and all the loadings are cyclic variation and the two types of mechanical loadings counter each other.

Consequently, it can be concluded that the rippled surface geometry and periodical residual stress distribution obtained from the machining process giving rise to segmented chip are primarily related to the cyclical variation of the mechanical and thermal loadings acting on the machined surface.

4.2.3 Analysis of single segment chip generation

It is known that the thin ploughed layer of material has the main contribution to plastic deformation and residual stress of the machined component. As shown in Fig. 12, stagnation point S is the place where the actual separation area of the material. The material in front of the edge radius would flow into two ways; either to be pushed upwards to generate chip or to be ploughed into newly machined surface in the condition of high transient stress, large strains and strain rates in high temperature. For this

reason, the two friction stress (τ_{SA} and τ_{SC}) oppose each other on opposite sides of stagnation point S. During the cutting process, the material in front of the tool tip experiences severe compressive pressure exerted by the tool tip and shear plane, having a tendency to generate tensile residual stress. As the tool progresses, some portion of this area is ploughed into the newly machined surface and thus subjected to stretching exerted by flank face SC, having a trend to produce compressive residual stress. However, the thermal loading will result in tensile residual stress on the machined surface due to inhomogeneous distribution of temperature. Therefore, the final residual stress distribution in the surface/near surface layer will be the combination of the above-mentioned two effects (plastic deformation caused by mechanical and thermal loadings).

When a segmented chip is produced, the cutting and feed forces show cyclical fluctuation, which will significantly affect the stress condition acting on the ploughed area, and thereby alter the residual stress state. In order to improve the understanding of how the segmented chip affects the cutting force and feed force, and further machined integrity, attention is focused on the steps portraying the generation of one chip segment during the cutting period from 380 to 560 µs.

Figure 13 gives the evolution of material degradation during one chip segment generation, presenting that the formation

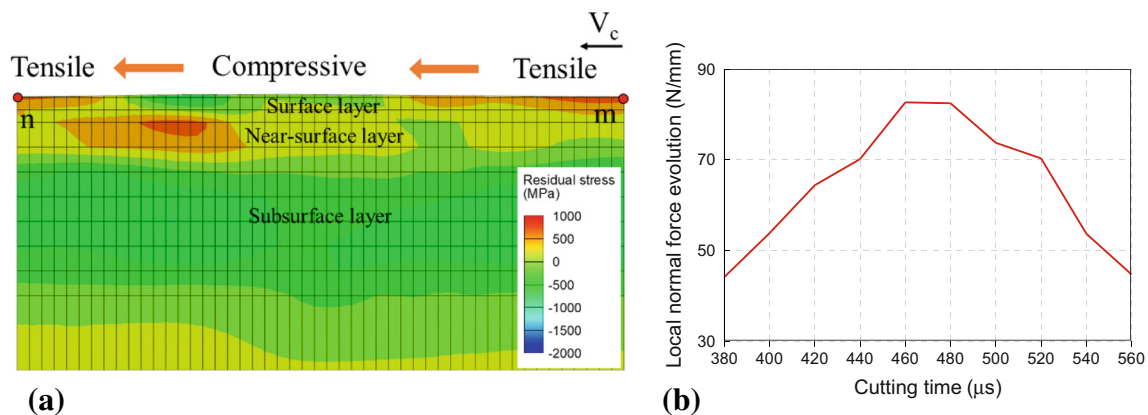


Fig. 14 (a) Residual stress distribution and (b) local normal force variation in the same time period

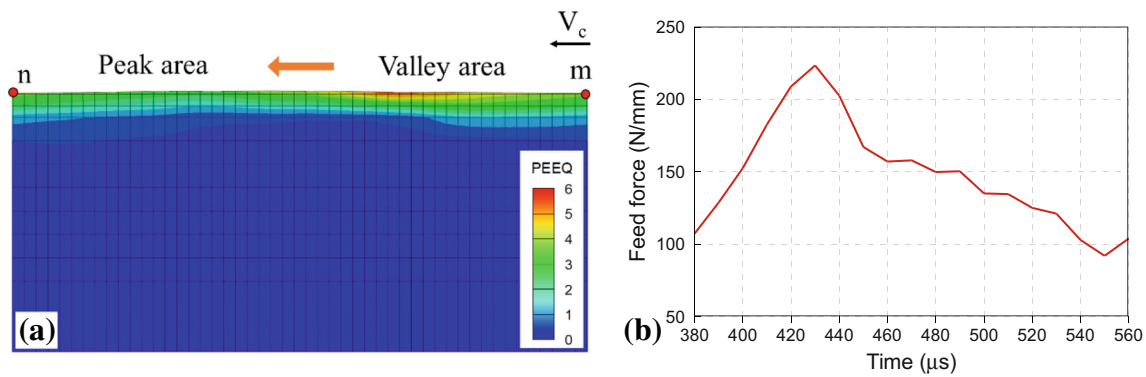


Fig. 15 (a) Plastic equivalent strain field and (b) feed force evolution in the same time period

of one segment includes two stages. The first stage takes place during 380 to 460 μs , in which the shear band starts at the tool tip and propagates toward the chip free surface with the advancement of the tool. At this stage, a decrease in cutting force is to be noted due to a loss in material stiffness propagating through shear band, while the feed force increases as a counter effect. The second stage characterizing the upward movement of the generated shear band along the tool rake face occurs from 460 to 560 μs of the cutting time. In this period, the cutting force recovers resulting from the transferring damaged material, and, on the contrary, a reduction of feed force is found, which can be backed by the evolution of cutting force and feed force in this time period (Fig. 7).

Figure 14a shows the generated residual stress distribution during this time period before the workpiece cooling down. The residual stress from location m to n corresponds to the cutting time from 380 to 560 μs . As mentioned before, the extrusion and friction between flank face and newly machined surface is the dominating reason causing surface compressive residual stress. Therefore, the local normal force variation acting on the SC part of the tool during the same time period is shown in Fig. 14b. An increase in local normal force is noticed during stage 1, which is due to the increased feed force in this period as mentioned previously, and vice versa for stage 2. It can be deduced that when the local normal force is relatively lower, the friction force applied on the new machined surface is weakened and thus more tensile residual stress is produced at the surface/near surface layer. With the increase in the local normal force, the material below the tool edge is stretched more severely and thus more compressive residual stress is generated in the surface layer. It is known that the compressive residual stress in the subsurface layer is caused by the mechanical effect during machining [45]. Therefore, in order to maintain an equilibrium state, the corresponding tensile residual stress is generated in the near-surface layer when the local normal force shows a higher value. It is also expected that the high temperature would cause more tensile residual stress in the surface/near surface layer after the material is cooled down.

The feed force is believed as a dominant factor in terms of the surface profile, and Fig. 15 shows the plastic equivalent

strain on the machined surface and feed force evolution in this time period that the plastic equivalent strain field from location m to n corresponds to the cutting time from 380 to 560 μs . It can be seen that a valley-shaped zone along with a larger material deformation is formed with a larger feed force. While a peaked location with a smaller value of plastic equivalent strain is generated when the feed force drops.

5 Conclusions

The CEL formulation-based two-dimensional finite element model has been developed to investigate the influence of segmented chip morphology in the machining of Inconel718 with uncoated carbide inserts. The simulation results with fine mesh show a good agreement with the experimental chip morphology, temperature distribution, cutting forces, residual stress profile and surface fluctuation period. In addition, the effects of the segmented chip morphology on the residual stress distribution and machined surface topography are discussed. The major conclusions can be summarized as follows:

1. The element (mesh) size has a significant influence on the chip morphology, indicating that a proper mesh size should be selected to get appropriate simulated segmented chips and accurate simulation of surface. For the coarse mesh (35 μm), a rough and continuous chip is observed, and the character of segmented chip starts to appear at the coarse mesh (10 μm) although it is not evident, while the fine mesh (5 μm) leads to a well-segmented chip in line with the experiment results.
2. A rough surface and cyclic residual stress distribution are generated on the machined workpiece when a segmented chip is formed. Effect of the segmented chip on surface integrity is attributed to the periodical change of mechanical and thermal loadings on the machined surface during chip segment generation.
3. The local normal force acting on the tool flank face increases at first and then decreases in the formation of a

single segment chip. Compressive residual stress is produced on the machined surface when it experiences severe stretching under a higher local normal force, while the residual stress in near-surface layer is more tensile. It has also been found that, when local normal force is lower, more tensile residual stress is produced in the surface/near-surface layer. Compressive residual stress is generated in the subsurface layer due to the mechanical effect during machining. In addition, the machined surface topography and plastic deformation are determined by feed force evolution with segment genesis.

Acknowledgement The authors would like to thank Dr. Rachid M'Saoubi and Mr. Per-Ola Jonander for support in the preparation of the experiment during the investigation and constructive discussion with them. One of the authors (Y. Liu) appreciates the financial support by the China Scholarship Council (No. 201706130144).

Funding Information Open access funding provided by Lund University.

Open Access This article is licensed under a Creative Commons Attribution 4.0 International License, which permits use, sharing, adaptation, distribution and reproduction in any medium or format, as long as you give appropriate credit to the original author(s) and the source, provide a link to the Creative Commons licence, and indicate if changes were made. The images or other third party material in this article are included in the article's Creative Commons licence, unless indicated otherwise in a credit line to the material. If material is not included in the article's Creative Commons licence and your intended use is not permitted by statutory regulation or exceeds the permitted use, you will need to obtain permission directly from the copyright holder. To view a copy of this licence, visit <http://creativecommons.org/licenses/by/4.0/>.

References

- Ozel T, Llanos I, Soriano J, Arrazola P-J (2011) 3D finite element modelling of chip formation process for machining Inconel 718: comparison of FE software predictions. *Mach Sci Technol* 15:21–46. <https://doi.org/10.1080/10910344.2011.557950>
- Calamaz M, Coupard D, Girod F (2008) A new material model for 2D numerical simulation of serrated chip formation when machining titanium alloy Ti–6Al–4V. *Int J Mach Tools Manuf* 48:275–288. <https://doi.org/10.1016/j.ijmactools.2007.10.014>
- Ducobu F, Rivière-Lorphève E, Filippi E (2014) Numerical contribution to the comprehension of saw-toothed Ti6Al4V chip formation in orthogonal cutting. *Int J Mech Sci* 81:77–87. <https://doi.org/10.1016/j.ijmecsci.2014.02.017>
- Agmell M, Ahadi A, Zhou JM, Peng RL, Bushlya V, Ståhl JE (2017) Modeling subsurface deformation induced by machining of Inconel 718. *Mach Sci Technol* 21:103–120. <https://doi.org/10.1080/10910344.2016.1260432>
- Özel T (2009) Computational modelling of 3D turning: influence of edge micro-geometry on forces, stresses, friction and tool wear in PcBN tooling. *J Mater Process Technol* 209:5167–5177. <https://doi.org/10.1016/j.jmatprotec.2009.03.002>
- Agmell M, Ahadi A, Gutnichenko O, Ståhl J-E (2017) The influence of tool micro-geometry on stress distribution in turning operations of AISI 4140 by FE analysis. *Int J Adv Manuf Technol* 89: 3109–3122. <https://doi.org/10.1007/s00170-016-9296-7>
- Sartkulvanich P, Altan T, Göcmen A (2005) Effects of flow stress and friction models in finite element simulation of orthogonal cutting—a sensitivity analysis. *Mach Sci Technol* 9:1–26. <https://doi.org/10.1081/MST-200051211>
- Pu Z, Umbrello D, Dillon OW, Jawahir IS (2014) Finite element simulation of residual stresses in cryogenic machining of AZ31B Mg alloy. *Procedia CIRP* 13:282–287. <https://doi.org/10.1016/j.procir.2014.04.048>
- Jafarian F, Imaz Ciaran M, Umbrello D, Arrazola PJ, Filice L, Amirabadi H (2014) Finite element simulation of machining Inconel 718 alloy including microstructure changes. *Int J Mech Sci* 88:110–121. <https://doi.org/10.1016/j.ijmecsci.2014.08.007>
- Huang JM, Black JT (1996) An evaluation of chip separation criteria for the FEM simulation of machining. *J Manuf Sci Eng* 118:545–554. <https://doi.org/10.1115/1.2831066>
- Grissa R, Zemzemi F, Fathallah R (2018) Three approaches for modeling residual stresses induced by orthogonal cutting of AISI316L. *Int J Mech Sci* 135:253–260. <https://doi.org/10.1016/j.ijmecsci.2017.11.029>
- Bäker M, Rösler J, Siemers C (2002) A finite element model of high speed metal cutting with adiabatic shearing. *Comput Struct* 80:495–513. [https://doi.org/10.1016/S0045-7949\(02\)00023-8](https://doi.org/10.1016/S0045-7949(02)00023-8)
- Klocke F, Raedt H-W, Hoppe S (2001) 2D-FEM simulation of the orthogonal high speed cutting process. *Mach Sci Technol* 5:323–340. <https://doi.org/10.1081/MST-100108618>
- Xie JQ, Bayoumi AE, Zbib HM (1998) FEA modeling and simulation of shear localized chip formation in metal cutting. *Int J Mach Tools Manuf* 38:1067–1087. [https://doi.org/10.1016/S0890-6955\(97\)00063-1](https://doi.org/10.1016/S0890-6955(97)00063-1)
- Nasr MNA, Ng E-G, Elbestawi MA (2008) A modified time-efficient FE approach for predicting machining-induced residual stresses. *Finite Elem Anal Des* 44:149–161. <https://doi.org/10.1016/j.finel.2007.11.005>
- Muñoz-Sánchez A, Canteli JA, Cantero JL, Miguélez MH (2011) Numerical analysis of the tool wear effect in the machining induced residual stresses. *Simul Model Pract Theory* 19:872–886. <https://doi.org/10.1016/j.simpat.2010.11.011>
- Ben Moussa N, Sidhom H, Braham C (2012) Numerical and experimental analysis of residual stress and plastic strain distributions in machined stainless steel. *Int J Mech Sci* 64:82–93. <https://doi.org/10.1016/j.ijmecsci.2012.07.011>
- Miguélez MH, Zaera R, Molinari A, Cheriguene R, Rusinek A (2009) Residual stresses in orthogonal cutting of metals: the effect of thermomechanical coupling parameters and of friction. *J Therm Stress* 32:269–289. <https://doi.org/10.1080/01495730802637134>
- Nasr MNA, Ng E-G, Elbestawi MA (2007) Modelling the effects of tool-edge radius on residual stresses when orthogonal cutting AISI 316L. *Int J Mach Tools Manuf* 47:401–411. <https://doi.org/10.1016/j.ijmactools.2006.03.004>
- Madhavan V, Adibi-Sedeh AH (2005) Understanding of finite element analysis results under the framework of Oxley's machining model. *Mach Sci Technol* 9:345–368. <https://doi.org/10.1080/10910340500196587>
- Agmell M, Bushlya V, Laakso SVA, Ahadi A, Ståhl J-E (2018) Development of a simulation model to study tool loads in pcBN when machining AISI 316L. *Int J Adv Manuf Technol* 96:2853–2865. <https://doi.org/10.1007/s00170-018-1673-y>
- Ducobu F, Rivière-Lorphève E, Filippi E (2016) Application of the coupled Eulerian-Lagrangian (CEL) method to the modeling of orthogonal cutting. *Eur J Mech - A/Solids* 59:58–66. <https://doi.org/10.1016/j.euromechsol.2016.03.008>
- Ducobu F, Arrazola P-J, Rivière-Lorphève E, de Zarate GO, Madariaga A, Filippi E (2017) The CEL method as an alternative to the current modelling approaches for Ti6Al4V orthogonal cutting. *Procedia CIRP* 58:245–250. <https://doi.org/10.1016/j.procir.2017.03.188>

24. Klocke F, Döbbeler B, Peng B, Lakner T (2017) FE-simulation of the cutting process under consideration of cutting fluid. *Procedia CIRP* 58:341–346. <https://doi.org/10.1016/j.procir.2017.03.235>
25. Ducobu F, Rivière-Lorphève E, Filippi E (2017) Finite element modelling of 3D orthogonal cutting experimental tests with the coupled Eulerian-Lagrangian (CEL) formulation. *Finite Elem Anal Des* 134:27–40. <https://doi.org/10.1016/j.finel.2017.05.010>
26. Xu D, Liao Z, Axinte D, Sarasua JA (2020) Investigation of surface integrity in laser-assisted machining of nickel based superalloy. *Mater Des* 108851. <https://doi.org/10.1016/j.matdes.2020.108851>
27. Su G, Liu Z, Li L, Wang B (2015) Influences of chip serration on micro-topography of machined surface in high-speed cutting. *Int J Mach Tools Manuf* 89:202–207. <https://doi.org/10.1016/j.ijmactools.2014.10.012>
28. Chen L, El-Wardany TI, Harris WC (2004) Modelling the effects of flank wear land and chip formation on residual stresses. *CIRP Ann* 53:95–98. [https://doi.org/10.1016/S0007-8506\(07\)60653-2](https://doi.org/10.1016/S0007-8506(07)60653-2)
29. Mabrouki T, Girardin F, Asad M, Rigal J-F (2008) Numerical and experimental study of dry cutting for an aeronautic aluminium alloy (A2024-T351). *Int J Mach Tools Manuf* 48:1187–1197. <https://doi.org/10.1016/j.ijmactools.2008.03.013>
30. Ducobu F, Rivière-Lorphève E, Filippi E (2017) Mesh influence in orthogonal cutting modelling with the coupled Eulerian-Lagrangian (CEL) method. *Eur J Mech - A/Solids* 65:324–335. <https://doi.org/10.1016/j.euromechsol.2017.05.007>
31. Atlati S, Haddag B, Nouari M, Zenasni M (2011) Analysis of a new segmentation intensity ratio “SIR” to characterize the chip segmentation process in machining ductile metals. *Int J Mach Tools Manuf* 51:687–700. <https://doi.org/10.1016/j.ijmactools.2011.05.007>
32. Zhang Y, Mabrouki T, Nelias D, Gong Y (2011) FE-model for titanium alloy (Ti-6Al-4V) cutting based on the identification of limiting shear stress at tool-chip interface. *Int J Mater Form* 4:11–23. <https://doi.org/10.1007/s12289-010-0986-7>
33. Guo YB, Wen Q, Woodbury KA (2006) Dynamic material behavior modeling using internal state variable plasticity and its application in hard machining simulations. *J Manuf Sci Eng* 128:749–759. <https://doi.org/10.1115/1.2193549>
34. Chen G, Li J, He Y, Ren C (2014) A new approach to the determination of plastic flow stress and failure initiation strain for aluminum alloys cutting process. *Comput Mater Sci* 95:568–578. <https://doi.org/10.1016/j.commatsci.2014.08.029>
35. Johnson G, Cook W (1983) A constitutive model and data for materials subjected to large strains, high strain rates, and high temperatures. *Proc 7th Inf Sympo Ballist* 21:541–547
36. Iturbe A, Giraud E, Hormaetxe E, Garay A, Germain G, Ostolaza K, Arrazola PJ (2017) Mechanical characterization and modelling of Inconel 718 material behavior for machining process assessment. *Mater Sci Eng A* 682:441–453. <https://doi.org/10.1016/j.msea.2016.11.054>
37. Johnson G, Cook W (1985) Fracture characteristics of three metals subjected to various strains, strain rates and temperatures and pressures. *Eng Fract Mech* 21(1):31–48
38. Hillerborg A, Modéer M, Petersson P-E (1976) Analysis of crack formation and crack growth in concrete by means of fracture mechanics and finite elements. *Cem Concr Res* 6:773–781. [https://doi.org/10.1016/0008-8846\(76\)90007-7](https://doi.org/10.1016/0008-8846(76)90007-7)
39. Umbrello D (2008) Finite element simulation of conventional and high speed machining of Ti6Al4V alloy. *J Mater Process Technol* 196:79–87. <https://doi.org/10.1016/j.jmatprotec.2007.05.007>
40. Zorev NN (1963) Inter-relationship between shear processes occurring along tool face and shear plane in metal cutting. *Int Res Prod Eng* 49:143–152
41. Artozoul J, Lescalier C, Bomont O, Dudzinski D (2014) Extended infrared thermography applied to orthogonal cutting: mechanical and thermal aspects. *Appl Therm Eng* 64:441–452. <https://doi.org/10.1016/j.applthermaleng.2013.12.057>
42. Thakur DG, Ramamoorthy B, Vijayaraghavan L (2009) Study on the machinability characteristics of superalloy Inconel 718 during high speed turning. *Mater Des* 30:1718–1725. <https://doi.org/10.1016/j.matdes.2008.07.011>
43. Cakir FH, Gurgen S, Sofuoğlu MA, Celik ON, Kushan MC (2015) Finite element modeling of ultrasonic assisted turning of Ti6Al4V alloy. *Procedia - Soc Behav Sci* 195:2839–2848. <https://doi.org/10.1016/j.sbspro.2015.06.404>
44. Laakso SVA, Zhao T, Agmell M, Hrechuk A, Ståhl J-E (2017) Too sharp for its own good—tool edge deformation mechanisms in the initial stages of metal cutting. *Procedia Manuf* 11:449–456. <https://doi.org/10.1016/j.promfg.2017.07.135>
45. Jacobus K, DeVor RE, Kapoor SG (2000) Machining-induced residual stress: experimentation and modeling. *J Manuf Sci Eng* 122: 20. <https://doi.org/10.1115/1.538906>

Publisher's note Springer Nature remains neutral with regard to jurisdictional claims in published maps and institutional affiliations.